

A deep-learning-boosted surrogate model of a metal foam based protonic ceramic electrolysis cell stack for uncertainty quantification

Zheng Li^{a,b}, Chen Wang^a, Xi Chen^a, Na Yu^a, Lei Xing^{b,1}, Jin Xuan^{b,1}, Minfang Han^{c,1}, Meng Ni^{a,*}

^a Department of Building and Real Estate, Research Institute for Sustainable Urban Development (RISUD) & Research Institute for Smart Energy (RISE), The Hong Kong Polytechnic University, Hung Hom, Kowloon, Hong Kong, China

^b School of Chemistry and Chemical Engineering, Faculty of Engineering and Physical Sciences, University of Surrey, UK

^c Department of Energy and Power Engineering, Tsinghua University, Beijing 100084, China



ARTICLE INFO

Keywords:

Metal foam
Hydrogen production
Uncertainty quantification
Polynomial Chaos Expansion, Deep neural network

ABSTRACT

Protonic ceramic electrolysis cells (PCECs) are widely considered as an emerging technology that shows capability for enabling environmentally friendly large-scale production of hydrogen. PCEC stacks' performance is considerably lower compared to smaller, lab-scale button cells. This performance gap is largely attributed to the highly uneven distribution of reactants throughout the larger cell or stack, which presents a significant challenge to the development of PCEC stack. The issue of non-uniform reactant distribution in PCEC stacks can be effectively addressed by incorporating metal foam structures to replace the conventional rib design of the inter-connect components. A 3D multiphysical model is developed to train a deep-learning-boosted surrogate model for PCEC with metal foam, which is subsequently used for parameter screening and sensitivity analysis. A collection of 12 inputs that encompass operating/structural/microstructural/material parameters are chosen, in which the operating parameters are identified as influential parameters. Three distribution uniformity indices maintain strong consistence to variations in the inputs, implying the positive role of metal foam. Faradaic efficiency (FE) is primarily influenced by the operating voltage with a total Sobol index of 0.6. The current density and FE are determined as the most stable performance indicators, exhibiting standard deviations of 0.15 and 0.81 respectively. According to a safety threshold of 10 K cm^{-1} for temperature gradient, the probability of the stack operating below this threshold is 88.61 %. Valuable insights into the design and performance of PCEC stacks that incorporate metal foam structures are provided. The workflow developed in this work can be further leveraged to explore and optimize PCECs.

1. Introduction

Hydrogen is capable to serve as a pivotal role in addressing climate change due to its clean and renewable characteristics [1]. Compared with the traditional steam reforming method, utilizing renewable energy sources to power the electrochemical process for hydrogen production emerges as a more favourable and promising strategy [2–4]. This approach possesses higher efficiency and carbon inexpensive, making it a compelling solution for sustainable and green hydrogen production [5,6]. Protonic ceramic electrolysis cells (PCECs) integrated with wind or solar power are efficient electrochemical devices for the large-scale production of clean hydrogen [7]. It also holds promise as a

potential solution to drive the realization of a green hydrogen future [8,9]. However, the development of PCECs faces significant constraints, particularly related to their anode performance. In a conventional PCEC stack, the anode thickness typically falls within the range of 20–40 μm [10–12]. This anode design makes the steam distribution in PCEC non-uniform. Thus, PCEC performance can be reduced. An equivalent observation is noted in SOECs and PEMECs as well [13–17]. To addressing this challenge, the application of metal foam replacing the function of the anode flow channel in the electrolysis cells is a promising solution. Its impact on both solid oxide electrolysis cells (SOECs) and proton exchange membrane electrolysis cells (PEMECs) has been extensively outlined in many experimental and numerical studies. The study by Toghyani et al. [18] presented a 3D PEMEC model. The results

* Corresponding author.

E-mail address: meng.ni@polyu.edu.hk (M. Ni).

¹ These authors contribute equally.

Nomenclature	
Abbreviation	
RMSE	Root-mean-square error
YSZ	Yttria-stabilized zirconia
BZY	Yttrium-doped barium zirconate
PCEC	Protonic ceramic electrolysis cell
PCE	Polynomial Chaos Expansion
DNN	Deep neural network
PDF	Probability density function
FE	Faradaic efficiency
MOAT	Morris-one-at-a-time
EE	Elementary effect
SI	Sobol index
R ²	R-squared
<i>Letter</i>	
<i>i</i>	Current density (A m^{-2})
η_{act}	Activation loss (V)
<i>T</i>	Absolute temperature, K
<i>F</i>	Faraday constant, $96485.3 \text{ C mol}^{-1}$
γ_0	Pre-exponential factor of exchange current density
<i>p_i</i>	partial gas pressure (Pa)
<i>E_{act}</i>	Activation energy, J mol^{-1}
<i>E_{eq}</i>	Equilibrium potential (V)
η	Overpotential (V)
α	Coefficient of charge-transfer
ϕ_{el}	Electrostatic potential, V
<i>n</i>	Number of electrons transferred
<i>p_i^{TPB}</i>	Partial pressure at triple-phase boundaries (Pa)
<i>E⁰</i>	Standard potential (V)
ΔG	The change in Gibbs energy (J mol^{-1})
<i>i₀</i>	Exchange current density (A m^{-2})
<i>J_i</i>	Molar flux of species <i>i</i> ($\text{mol m}^{-2} \text{ s}^{-1}$)
z_i	Number of charges
ϵ_{abs}	Absolute permittivity (F m^{-1})
OH_O	Protonic defects
D^{eff}	Effective coefficient
V_O^{\cdot}	Oxygen vacancies
O_O	Electronic holes
s_d	The source of defect reaction
O_O^{\times}	Lattice oxygen
V_m	Molar volume, $\text{m}^3 \text{ mol}^{-1}$
[d]	Defects concentration (mol m^{-3})
ρ	Density, kg m^{-3}
M_i	Molar mass of species <i>i</i> , kg mol^{-1}
ω_i	Mass fraction of species <i>i</i>
[d] _L	Unit concentration
\mathbf{i}_e	Electronic current vector
K_{eq}	Equilibrium constant
σ_0	Intrinsic conductivity, S m^{-1}
ζ	Bruggeman factor
φ_e	Electrical potential, V
V_s	Volume fraction
P_{per}	Percolation probability
\mathbf{u}	Velocity, m/s
\mathbf{N}_i	Molar flux of species <i>i</i> , $\text{mol m}^{-2} \text{ s}^{-1}$
C_p	Thermal capacity, $\text{J kg}^{-1} \text{ K}^{-1}$
λ_{eff}	Effective thermal conductivity, $\text{W m}^{-1} \text{ K}^{-1}$
Q_i	Source term <i>i</i>
ε	Porosity of the porous electrode
d_p^{eff}	Effective pore diameter, m
d_p	Pore diameter, m
Γ_q	Distribution uniformity index
\mathbf{X}	Vector of inputs
$f(\mathbf{X})$	Probability density function
\mathbf{Y}	Vector of outputs
c_a	Expansion coefficients
μ	Viscosity, Pa s
$\Psi_a(\mathbf{X})$	Orthogonal polynomials
τ	Tortuosity of the porous electrode
<i>Subscript</i>	
ede	Porous electrode
mf	Metal foam

from this model indicated that a PEMEC design incorporating metal foam outperformed the traditional PEMEC configuration. Wei et al. [19] numerically demonstrated a 13 % improvement of temperature uniformity in a metal foam based PEMEC. Wan et al. [20] conducted experimental investigations on metal foam based PEMFC, demonstrating its capability to reduce temperature difference in the cell. Zhao et al. [21] reported that a 10 % enhancement of steam diffusion in the anode of metal foam based SOEC. Wang et al. [22] numerically revealed that using metal foam in a co-electrolysis SOEC significantly reduces the temperature gradient. The work by Zielke et al. [23] provided experimental validation of the beneficial impact of using metal foam in solid oxide cell stacks. Furthermore, the study by Han et al. [24] examined the influences of metal foam in a carbon-assisted SOEC, and reported a 70 % reduction in the maximum thermal stress. These studies collectively emphasize the beneficial role of metal foam in enhancing the performance and thermal characteristics of both SOECs and PEMECs. Thus, it is reasonable to anticipate a comparable positive effect of metal foam on PCECs.

Besides, not only operating parameters and material parameters but also the structural and microstructural parameters can influence the performance of a PCEC stack using metal foam. Understanding how the values of intrinsic/extrinsic parameters impact metal foam based PCEC's performance and how their variations affect the stability of PCEC performance is an important area of investigation. Particularly, the current

leakage phenomenon in PCEC is a remarkable challenge [25,26]. The current leakage can lead to a reduction in faradaic efficiency (FE) and decrease the PCEC's hydrogen production capability. Given the potential benefits of metal foam-based designs, the understanding on how input parameters affect the FE in a PCEC incorporating metal foam is important. Previous research has shown that sensitivity analysis (SA) and uncertainty quantification (UQ) techniques can significantly contribute to a better comprehension of the influence of these parameters. The study by Karyofylli et al. [27] presented a model framework that coupled quasi-Monte Carlo (MC) and polynomial chaos expansion (PCE) approaches to perform uncertainty quantification in a PEMEC model. The operating voltage is found to be highly sensitive to the membrane thickness. Kannan et al. [28] performed a UQ on a PEMFC using MC method and a machine learning based surrogate model. The correlation between 33 inputs and 3 outputs were unveiled. Shao et al. [29] selected a set of 19 input parameters to perform SA on SOFCs. By employing their machine learning assisted PCE surrogate model, the most important parameters that significantly affect three specific overpotentials in SOFC were pinpointed. In addition, Radaideh et al. [30] proposed a framework integrating SA and UQ to investigate SOFC based on 21 inputs. Results suggested that the operating temperature accounts for more than 60 % of the variation of the maximum power in SOFC. The work by Gholaminezhad et al. [31] utilized the MC method to assess the robustness of the optimal design point, which is obtained from their

SOFC model. Similarly, another work employed the MC method to quantify the robustness of a SOEC model [32].

As a result, to acquire such a comprehension for a PCEC stack, a framework of this study is illustrated in Fig. 1. Initially, a detailed 3D model of a PCEC stack is presented. As shown in the fish-bone diagram, a set of 12 operating, structural, microstructural, and material input parameters are selected. Additionally, a set of 8 parameters are chosen as performance indicators. The previous studies demonstrate the effectiveness of the PCE surrogate model as a powerful tool for performing SA and UQ in the context of SOFC/SOEC systems. However, as highlighted in previous research [33], a major challenge in developing PCE model lies in the computation of PCE coefficients, primarily due to the high-dimensional nature stemming from the increasing number of input parameters. For example, in this work, there are 126 coefficients of PCE surrogate model for each output. Therefore, this is a high-dimensional problem to build this PCE system. In this study, the PCE surrogate model for each output involves a substantial number of coefficients, totalling 126 coefficients. Consequently, constructing this PCE system becomes a high-dimensional problem. To tackle this challenge, deep neural networks (DNNs) are employed, leveraging their well-established ability to effectively handle high-dimensional systems [34]. Furthermore, a study led by Yao et al. [35] has showed the potential of utilizing DNNs to address the high-dimensional problem in PCE models by determining the coefficients. This work highlights the effectiveness of DNNs in mitigating the computational challenges associated with high-dimensional PCE models, offering a promising approach for handling such complexities. In this study, a similar approach is adopted by utilizing deep learning techniques to enhance the training of the PCE model. It is crucial to highlight that alternative machine learning techniques like Support Vector Regression (SVR) have demonstrated to be effective in managing regression duties and tackling high-dimensional challenges [36,37]. In future work, it would be valuable to investigate and compare the performance of SVR and DNN in enhancing the training of the PCE model. This comparative analysis would provide insights into the strengths and limitations of each approach and help determine the most suitable method for addressing the high-dimensional challenges associated with the PCE model. The numerical model serves as the basis for generating a dataset that includes input parameters and corresponding output values for training the deep neural network (DNN)

boosted PCE surrogate model. To attain a comprehensive comprehension of inputs' impacts, a three-step procedure is undertaken (shown in Fig. 1): 1) Parameter Screening: evaluate each input, thereby identifying and screening out the influential inputs/outputs. 2) Sensitivity Analysis: precisely quantify the impacts of crucial inputs on the outputs. 3) Uncertainty analysis: obtain the density estimates of outputs to the variations in the input parameters. In this study, Fig. 1 illustrates the utilization of a PCE surrogate model in a three-step parametric study. The three steps include parameter screening, sensitivity analysis, and uncertainty quantification. The primary motivation for employing the PCE model is to expedite the three-step parametric study, as the computational cost of the 3D model is significantly higher compared to the PCE model. By using the PCE model, predictions of PCEC stack performance can be achieved without incurring the high computational expenses associated with the 3D numerical model. This work aims to gain a deep understanding of the impacts of different factors on stacks with metal foam. Conducting a sensitivity analysis allows for quantitatively assessing the impacts of several inputs on PCECs. By employing the PCE model for sensitivity analysis, this process can be accelerated, reducing computational costs while still presenting valuable perceptions into the different factors' impacts on PCECs. Overall, this 3D model provides valuable insights into how the performance of a metal foam-based PCEC stack is affected by variations in the input parameters. This makes a significant contribution to the development of PCEC technology for hydrogen production.

2. Simulation methodology

In this section, the simulation domain of the PCEC stack is introduced, along with the main governing equations used to describe the operation of the PCEC stack. The surrogate model development and the workflow of performing the parameter screening are also described briefly. The 3D numerical model solves a series of partial differential equations depicting the intricate processes occurring in the PCEC stack. However, the 3D geometry of the stack adds complexity and increases the time required for solving the multiphysics model. Obtaining a single numerical solution demands a minimum of 20 min of CPU time. In contrast, a well-trained PCE surrogate model can provide output predictions in less than 1 s. Consequently, using the PCE surrogate model

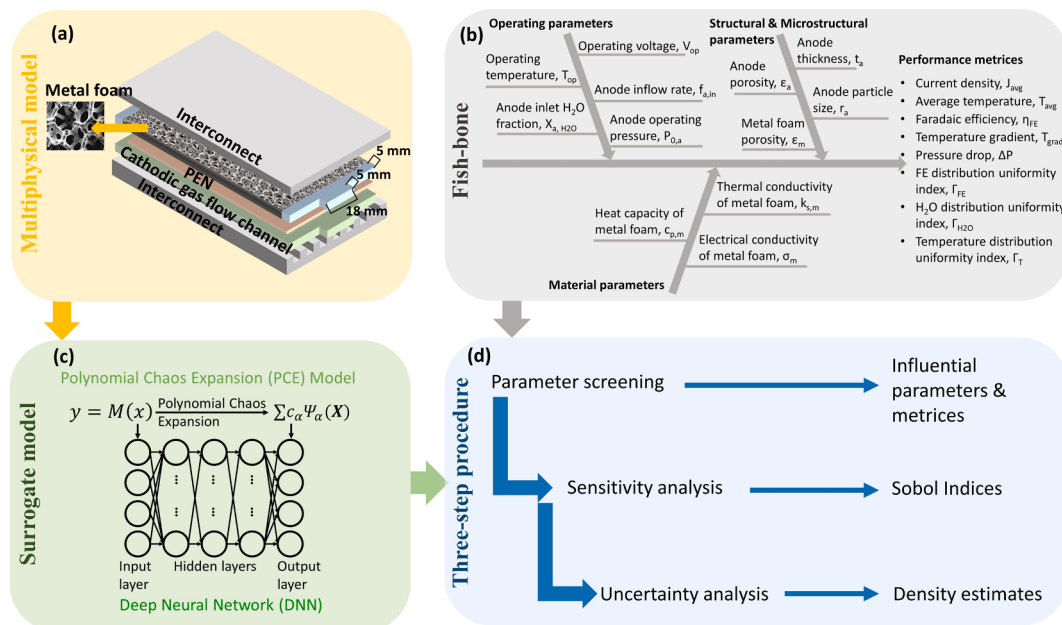


Fig. 1. Schematics of the framework (a) 3D geometry of numerical model; (b) fish-bone diagram of 12 inputs and 8 outputs; (c) structure of surrogate model; (d) the three-step procedure.

for PCEC's performance predictions is more effective than relying on the 3D numerical model. This approach significantly accelerates the SA and UQ processes, enabling faster analysis in evaluating PCEC performance.

2.1. Simulation domain

The geometry of the PCEC stack features a metal foam as the anode gas/current distributor (Fig. 1(a)). The thicknesses of the different components are: anode $-30\text{ }\mu\text{m}$, cathode $-500\text{ }\mu\text{m}$, electrolyte $-20\text{ }\mu\text{m}$, metal foam -1.5 mm , and interconnector -2 mm . The cell active area is $5 \times 5\text{ cm}^2$, and the cathode gas channel width and rib width are both 2 mm . Additional important parameters are listed in Table 2. The key assumptions made in the model are:

- 1) In this study, the fluid flow within the PCEC stack, $(\text{H}_2, \text{O}_2, \text{H}_2\text{O})$, is considered to be incompressible, since the pressure gradient along the gas channel is small ($<60\text{ Pa cm}^{-1}$). Additionally, the Mach number is found to be smaller than 0.01 in the PCEC stack. The assumption of incompressible fluid flow is widely utilized in other simulation studies as well [38,39]. Thus, adopting this assumption is reasonable and appropriate.
- 2) Both the anode and cathode consist of evenly distributed particles (electrolyte and electrode).
- 3) It is assumed that electrochemical reactions occur at the interface between the electrolyte and the electrode.
- 4) The mobile charge carriers in the electrolyte are protonic defects, oxygen vacancies, and electronic holes.
- 5) The defect reactions are in an equilibrium state.

The 8 outputs are collected in Table 1. Noteworthy, the distribution uniformity index (Γ_q) for the physical variable (q) can be calculated as [40]:

$$\Gamma_q = 1 - \left(\frac{\sum_{i=1}^n \left[\frac{q_i - \bar{q}}{\bar{q}} \right]^2}{n} \right)^{0.5} \quad (1)$$

2.2. Governing equations

In this section, the equations that are utilized to construct a stack model are presented. These equations are used to describe the complicated processes that occur within the PCEC stack.

2.2.1. Electrochemistry

The Butler-Volmer equation that describes the inter-relationship between the potential, current, and reaction kinetics is used to model the charge-transfer process, which is a key electrochemical phenomenon occurring within the PCEC stack [4,7]:

$$i = i_0 \left[\exp\left(\frac{\alpha F \eta_{act}}{RT}\right) - \exp\left(\frac{-(1-\alpha) F \eta_{act}}{RT}\right) \right] \quad (2)$$

Table 1
8 output parameters.

Parameters	Notations	Units
Current density	J_{avg}	A cm^{-2}
Faradaic efficiency	η_{FE}	%
Average temperature	T_{avg}	$^\circ\text{C}$
Temperature gradient	T_{grad}	K cm^{-1}
Pressure drop	ΔP	Pa
FE distribution uniformity	Γ_{FE}	1
Temperature distribution uniformity	Γ_T	1
H_2O distribution uniformity	Γ_{H2O}	1

Table 2
The model parameters applied in constructing three-dimensional model.

Parameters	Value/expression	Unit
σ_m	28540	S m^{-1}
$\varepsilon_{a/c}$	0.4	1
ε_m	0.8	1
$\tau_{a/c}$	3	1
$r_{particle}$	0.5	μm
$V_{f,a}$	0.6	1
$V_{f,c}$	0.6	1
$K_{s,m}$	72	$\text{W m}^{-1}\text{ K}^{-1}$
$C_{p,m}$	518	$\text{J kg}^{-1}\text{ K}^{-1}$

$$i_{0,a} = \gamma_{0,a} \exp\left(-\frac{E_{act,a}}{RT}\right) p_{O_2}^{0.25} p_{H_2O} \quad (3)$$

$$i_{0,c} = \gamma_{0,c} \exp\left(-\frac{E_{act,c}}{RT}\right) p_{H_2} \quad (4)$$

Noteworthy, the definition of each letter in the equations and their units can be found in nomenclature section. The operating voltage (V_{op}) of PCEC can be calculated as follows [41]:

$$V_{op} = E_{eq} + \eta_{act} + \eta_{ohmic} \quad (5)$$

$$E_{eq} = E^0 + \frac{RT}{nF} \ln \left[\frac{p_{H_2}^{TPB} (p_{O_2}^{TPB})^{0.5}}{p_{H_2O}^{TPB}} \right] = -\frac{\Delta G}{nF} + \frac{RT}{nF} \ln \left[\frac{p_{H_2}^{TPB} (p_{O_2}^{TPB})^{0.5}}{p_{H_2O}^{TPB}} \right] \quad (6)$$

2.2.2. Charge transfer

In the electrolyte of the PCEC stack, the Nernst-Planck equation models the flux and transport of ionic species within the electrolyte. This accounts for the movement and distribution of the charge carriers. The Poisson equation, on the other hand, relates the electrolyte potential (ϕ_{el}) to the charge carrier concentrations. This allows the model to capture the spatial distribution of the electrolyte potential throughout the PCEC stack [42,43]:

$$J_i = -D_i^{eff} (\nabla c_i + \frac{z_i F}{RT} c_i \nabla \phi_{el}) \quad (7)$$

$$\nabla \cdot (\epsilon_{abs} \nabla \phi_{el}) + F \sum_i z_i c_i = 0 \quad (8)$$

The equation that describes the conservation of different charged defects in the electrolyte layer of the PCEC stack model is shown as:

$$\nabla \cdot J_i = s_d \quad (9)$$

where s_d represents a source term in the equation that describes the conservation of charge carriers in the electrolyte. This source term accounts for the defect chemical reactions, which describe the inter-relationship between the gas phase species and the defect species present within the electrolyte material. In other words, s_d term captures the generation or consumption of charge carriers due to chemical reactions involving defects in the electrolyte [42]:



where O_2^\times denotes for the lattice oxygen site in the electrolyte material [44]. The equilibrium constant for each defect reaction in the PCEC stack electrolyte can be written as a function of the molar concentrations of the defect species and the partial pressures of the gas phase species [45]:

$$K_{p,H_2} = \frac{[OH_o]}{[O_o]p_{H_2}^{0.5}} \quad (13)$$

$$K_{p,H_2O} = \frac{[OH_o]^2}{[O_o^\times][V_o]p_{H_2O}} \quad (14)$$

$$K_{p,O_2} = \frac{[O_o]^2}{[O_o^\times][V_o]p_{O_2}^{0.5}} \quad (15)$$

where $[d]$ is the defect molar concentration (mol m^{-3}). The $[d]_L$, which is the unit concentration, can be expressed as the product of the molar concentration and the molar volume (V_m). Furthermore, the equilibrium constant can also be computed when the entropy change (ΔS°) and enthalpy change (ΔH°) are known:

$$K = \exp\left(\frac{\Delta S^\circ}{R}\right) \cdot \exp\left(-\frac{\Delta H^\circ}{RT}\right) \quad (16)$$

The thermodynamic data required to determine the equilibrium constants of the several reactions (between defects) in the PCEC stack can be found in Ref. [42]. Another two constraints are required for solving the concentration of different defects. One is electroneutrality, the other is the conservation of oxygen site in the electrolyte material.

$$[OH_o] + 2[V_o] + [O_o] - [Yb'_{Zr}] = 0 \quad (17)$$

$$[OH_o] + [V_o] + [O_o] + [O_o^\times] = 3 \quad (18)$$

Once the molar flux and concentration of charge carriers in the PCEC's electrolyte are determined, the current density and conductivity for each species, along with their sum, can be calculated as follows:

$$i_i = z_i F J_i \quad (19)$$

$$i_{ex} = F \sum_i z_i J_i = \sum_i i_i \quad (20)$$

$$\sigma_i = \frac{F^2}{RT} z_i^2 c_i D_i \quad (21)$$

$$D_i = D^0 \exp\left(-\frac{E_{act,d}}{RT}\right) \quad (22)$$

$$\sigma_{el} = \sum_i \frac{F^2}{RT} z_i^2 c_i D_i \quad (23)$$

Besides, the conduction of electrons in the electrode material and the effective electronic conductivity (σ_e^{eff} , S m^{-1}) are depicted [46–47]:

$$\nabla \cdot \mathbf{i}_e = \nabla \cdot (\sigma_e^{\text{eff}} \nabla \phi_e) \quad (24)$$

$$\sigma_{eff} = \sigma_0 [(1 - \epsilon) V_f P_{per}]^\zeta \quad (25)$$

2.2.3. Mass and momentum transfer

The transport of H_2 , H_2O , O_2 in the PCEC is described using the Dusty Gas Model (Eq. (26) [7]). Additionally, momentum transport in the PCEC is characterized by the Navier-Stokes equation adjusted with Darcy's term (Eq. (27), where the Darcy's term is omitted in the gas channel domain [48,49]):

$$\frac{\mathbf{N}_i}{D_{ik}^{\text{eff}}} + \sum_{j=1}^n \frac{y_j \mathbf{N}_i - y_i \mathbf{N}_j}{D_{ij}^{\text{eff}}} = -\frac{1}{RT} \left(P \nabla y_i + y_i \nabla P + y_i \nabla P \frac{kP}{D_{ik}^{\text{eff}} \mu} \right) \quad (26)$$

$$\frac{\rho}{\epsilon} (\mathbf{u} \cdot \nabla) \frac{\mathbf{u}}{\epsilon} = -\nabla P + \nabla \cdot \left[\frac{\mu}{\epsilon} (\nabla \mathbf{u} + \nabla \mathbf{u}^T) - \frac{2}{3} \frac{\mu}{\epsilon} (\nabla \cdot \mathbf{u}) \right] - \left(\mu \kappa^{-1} + \frac{Q_m}{\epsilon^2} \right) \mathbf{u} \quad (27)$$

$$\rho \nabla \cdot \mathbf{u} = \sum y_i R_i = Q_m \quad (28)$$

Noteworthy, the permeability (κ_{ede}) of porous electrode can be linked to its porosity (ϵ_{ede}) and pore diameter ($d_{p,ede}$) via the Carman-Kozeny correlation [40]. Moreover, the metal foam's permeability (κ_{mf}) can be determined from its microstructural characteristics based on the following formula [50]:

$$\kappa_{ede} = \frac{\epsilon_{ede}^3 d_{p,ede}^2}{180(1 - \epsilon_{ede})^2} \quad (29)$$

$$\frac{\kappa_{mf}}{d_{p,mf}^{\text{eff}}} = \frac{\epsilon_{mf}^2}{36\tau_{mf}(\tau_m - 1)} \quad (30)$$

$$d_{p,mf}^{\text{eff}} = d_{p,mf} \left(\frac{\tau_m}{\epsilon_m} \right)^{0.5} \quad (31)$$

$$\tau_{mf} = \left\{ \frac{3}{4\epsilon_{mf}} + \frac{\sqrt{9 - 8\epsilon_{mf}}}{2\epsilon_{mf}} \cos \left(\frac{4\pi}{3} + \frac{1}{3} \cos^{-1} \left(\frac{8\epsilon_{mf}^2 - 36\epsilon_{mf} + 27}{(9 - 8\epsilon_{mf})^{1.5}} \right) \right) \right\}^{-1} \quad (32)$$

2.2.4. Heat transfer

The energy conservation of PCEC is governed by the following equation [51]:

$$\rho C_{p,eff} \mathbf{u} \nabla T + \nabla \cdot (-K_{eff} \nabla T) = Q_h \quad (33)$$

2.2.5. Boundary conditions

Boundary conditions are listed in Table 3. The numerical model is solved using COMSOL Multiphysics, a platform that employs the finite element method to solve equations. With a total of 884,730 degrees of freedom (DOF), the independence of mesh is confirmed in this model. The model validation involves a comparison between simulation outcomes and experimental data. Fig. 2 demonstrates a robust correlation between the simulated results and the experimental observations.

2.3. Surrogate model

The configuration of the surrogate model can be observed in Fig. 1 (c). Polynomial chaos expansion (PCE) is a highly effective method for constructing surrogate models. When considering a model represented as $\mathbf{Y} = M(\mathbf{X})$, its polynomial expansion can be mathematically represented as [52]:

$$\mathbf{Y} = M(\mathbf{X}) = \sum c_a \Psi_a(\mathbf{X}) \quad (34)$$

where \mathbf{X} represents the input vector, defined by a joint probability

Table 3

Boundary conditions used in the 3D numerica.

Condition/Locations	Value	Unit
$x_{an,inlet}$	90 % $H_2O/10 \% O_2$	
$x_{ca,inlet}$	10 % $H_2O/90 \% H_2$	
$v_{an,inlet}$	6×10^{-5}	kg s^{-1}
$v_{ca,inlet}$	6×10^{-6}	kg s^{-1}
V_{op}	1.3	V
T_{op}	600	$^{\circ}\text{C}$
P_{op}	1	atm
Anode gas channel inlet	$x_{an,inlet}, v_{an,inlet}, T_{op}$	
Cathode gas channel inlet	$x_{ca,inlet}, v_{ca,inlet}, T_{op}$	
Anode side interconnector upper-face	$\varphi_e = V_{op}$	
Cathode side interconnector upper-face	$\varphi_e = 0$	
Outlet of anode gas channel	Open boundary	
Outlet of cathode gas channel	Open boundary	
Other boundaries	Insulation/Wall	

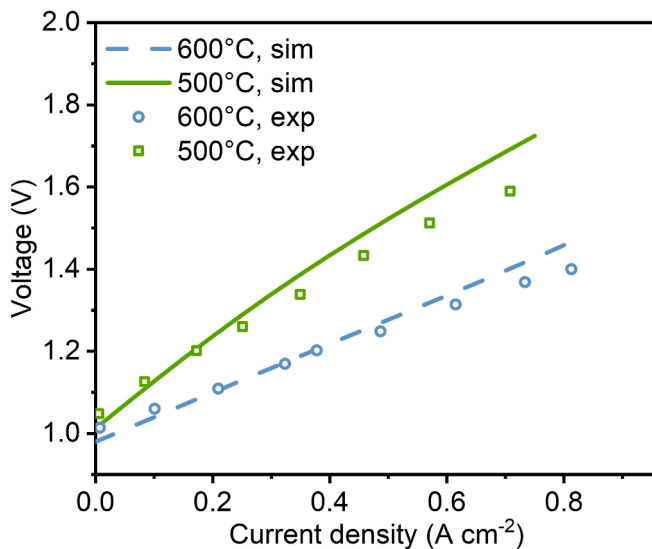


Fig. 2. Model validation.

density function (PDF, $f(\mathbf{X})$), \mathbf{Y} is output vector; c_α are the expansion coefficients; $\Psi_\alpha(\mathbf{X})$ are the orthogonal polynomial regarding $f(\mathbf{X})$ [53]:

$$\Psi_\alpha(\mathbf{X}) = \prod_{i=1}^M \psi_\alpha^i(x_i) \quad (35)$$

where M is the dimension of inputs. A total of 2^6 (64) samples are generated according to the predefined PDF and the specified value range as outlined in Table 4. In situations where detailed knowledge regarding the distribution of operating parameters for a PCEC stack is limited, assuming a uniform distribution is a straightforward and simple choice. Uniform distributions are particularly useful in SA as they allow for investigating the impact of varying a parameter across a specific range. By assuming a uniform distribution, one can explore the effects of operational parameter variations without making specific assumptions about the shape or characteristics of the distribution. Uniform distributions have also been utilized for performing UQ in SOFC, as demonstrated in Ref. [30]. It offers provides a flexible route to assess the influence of different operational parameter ranges on the PCEC stack's behaviour. In those samples, the outputs are calculated from the 3D numerical model. The dataset is randomly partitioned into two sets with a ratio of 0.8 to 0.2. In detail, the dataset splitting process utilize the torch.utils.data.random_split function in PyTorch to randomly divide the dataset into training and testing subsets. The function takes the original dataset and the desired sizes for the subsets, typically determined by a specified ratio. It then performs a random split, creating two new datasets: one for training and another for testing. These subsets

Table 4
12 input parameters.

Parameters, Notations, (Units)	PDFs	Ranges
Operating temperature, T_{op} , (V)	Uniform	[550, 600]
Operating voltage, V_{op} , (°C)	Uniform	[1.25, 1.45]
Anode inflow rate, $f_{a,in}$, (10^{-5} kg s ⁻¹)	Uniform	[6, 9]
Anode inlet H ₂ O fraction, X_{a, H_2O} , (1)	Uniform	[0.9, 0.99]
Anode operating pressure, $P_{o,a}$, (atm)	Uniform	[1, 5]
Anode porosity, ϵ_a , (1)	Uniform	[0.4, 0.6]
Anode thickness, t_a , (μm)	Uniform	[20, 40]
Anode particle size, r_a , (μm)	Uniform	[0.45, 0.55]
Metal foam porosity, ϵ_m , (1)	Uniform	[0.75, 0.85]
Thermal conductivity of metal foam, $K_{s,m}$, (W m ⁻¹ K ⁻¹)	Uniform	[64, 80]
Heat capacity of metal foam, $C_{p,m}$, (J kg ⁻¹ K ⁻¹)	Uniform	[466, 570]
Electrical conductivity of metal foam, σ_m , (S m ⁻¹)	Uniform	[25686, 31394]

maintain the correct proportion of samples from the original dataset. Subsequently, DataLoader objects can be created for each subset, enabling efficient loading of data during model training and evaluation. The training DataLoader typically includes shuffling of samples, while the testing DataLoader does not. This process ensures a representative split of the dataset, allowing for following training and evaluation of DNN model in PyTorch. A 4th order PCE model (126 coefficients) is constructed first. This model serves as a baseline for performance comparison. Subsequently, a DNN-boosted PCE model is developed. Noteworthy, three hidden layers (64-128-64) and ReLu activation function are utilized in the DNN model. Surrogate model's performance is calculated by utilizing two metrics. R-squared (R^2) and Root-mean-square error (RMSE) are employed to assess the effectiveness of surrogate model [54].

$$R^2 = 1 - \frac{SS_{res}}{SS_{tot}} = 1 - \frac{\sum (y_{real} - y_{pred})^2}{\sum (y_{real} - y_{mean})^2} \quad (36)$$

$$RMSE = \sqrt{\frac{1}{N} \sum (y_{real} - y_{pred})^2} \quad (37)$$

Table 5 presents the performance of two surrogate models. The results indicate that the DNN-boosted PCE model exhibits a slightly lower R^2 compared to the PCE model. However, it shows an improvement in RMSE. Overfitting poses a challenge during the development of the surrogate model. While cross-validation is an effective approach to mitigate this issue, in this study, L1 regularization is employed as a means to address overfitting in the process of developing the DNN model [55]. The loss function of DNN model add a L1 regularization term accounting for the sum of the absolute values of the model's parameters. Therefore, a DNN-boosted PCE model is used as the surrogate model for following studies.

2.4. Parameter screening

Morris (or one-at-a-time) method (MOAT) is employed to screen out parameters that exhibit no significance to the outputs [30]. MOAT calculates the elementary effect (EE) for each input factor for providing a quantitative measure of the significance of each input parameter.

$$Y = f(X_1, X_2, \dots, X_n, \dots, X_k) = f(\mathbf{X}) \quad (38)$$

$$EE_i = \frac{f(X_1, X_2, \dots, X_i + \Delta, \dots, X_k) - f(X_1, X_2, \dots, X_i, \dots, X_k)}{\Delta_i} \quad (39)$$

$$\mu_i^* = \frac{\sum_{j=1}^r |EE_i^j|}{r} \quad (40)$$

$$\sigma_i = \left[\frac{\sum_{j=1}^r (EE_i^j - \mu_i)^2}{r-1} \right]^{0.5} \quad (42)$$

where Y is the output, which is expressed as a function of k independent inputs; X_i is input i ($i = 1, 2, \dots, k$), outlining an input space with k -dimension that can be evenly organized to an L-level grid [56]; $\Delta_i =$

Table 5
Surrogate model performance.

Surrogate model	R ²	RMSE
PCE	0.997	0.436
DNN-boosted PCE	0.991	0.181

$\frac{L}{2(L-1)}$ stands for the spacing of the grid [57]; μ_i represents the mean value of EE, which signifies the overall impact of the input on the output; μ_i^* is the absolute mean value of EE; σ_i is the variance of EE, providing insights into the combined effects of the input, including its nonlinearity and interactions with other inputs [58].

3. Results and discussion

A detailed illustration and discussion of the results obtained from parameter screening, sensitivity analysis, and the performance distribution would be provided in this section. Those results could show how the surrogate model favour the understanding of metal foam based PCEC stack operation.

3.1. Parameter screening

The results of parameter screening are illustrated in both Fig. 3 and Fig. 4. To evaluate the impacts on an output parameter caused by the input, two values are typically obtained: MOAT mean (μ^*) and MOAT standard deviation (σ). Fig. 3(a) serves as an illustrative example to showcase how the MOAT mean and the MOAT standard deviation (σ) reveal the influence of an input on an output. Data points in Fig. 3(a) can be distinctly classified into three groups [59,60]: 1) Influential input parameters with non-interaction (V_{op} : the input parameters exhibit a relatively large value of MOAT mean and a relatively small value of MOAT standard deviation): a relatively large value of MOAT mean indicates that the magnitude of the elementary effects (influence) of these input parameters is large; a relatively small value of MOAT standard deviation indicates that the elementary effects of these input parameters exhibit low variation. 2) Influential input parameters with interaction (T_{op} : the input parameters exhibit a relatively large value of MOAT standard deviation and a relatively small value of MOAT mean): a relatively large value of MOAT standard deviation indicates that the elementary effects of these input parameters exhibit high variation (interactions with other parameters). 3) Non-influential input parameters ($X_{a,H2O}$, $P_{0,a}$, $k_{s,m}$, $c_{p,m}$, σ_m , ε_a , ε_m , r_a , t_a): the input parameters exhibit

relatively small value of both MOAT standard deviation and MOAT mean).

Despite having relatively small MOAT standard deviation and MOAT mean values, the $f_{a,in}$ parameter exhibits slightly higher values compared to the parameters in the non-influential group. As a result, it can be categorized as a less influential parameter. Therefore, the parameters, excluding those in the non-influential group, can be identified as the screened parameters from Fig. 3 and Fig. 4, which are collected into Table 6. The screened parameters are a subset of inputs exhibiting a notable impact on the performance indicators. These parameters are considered significant and can be further analysed or utilized for subsequent tasks. Furthermore, it is evident that the parameters listed in Table 6 are all operating parameters. Therefore, it may indicate that the PCEC's performance can be mainly controlled by operating parameters. This observation suggests that these parameters are important to affect the PCEC stack. As such, careful control and optimization of operating parameters are essential for achieving desired performance levels in metal foam based PCEC stack. Furthermore, it is worth mentioning that the MOAT standard deviation and MOAT mean values of different input parameters for the three uniformity indices are relatively small compared to other performance indicators. This suggests that these uniformity indices are highly stable and not very sensitive to changes in inputs. It also highlights the significant role of metal foam in enhancing the distribution uniformity in PCEC stacks. Based on this observation, it is reasonable to neglect these uniformity indices as performance indicators for following studies, as their stability and limited sensitivity to input parameter variations.

3.2. Sensitivity analysis

The significance of parameters can be quantified using the first-order Sobol index (SI_1) and total Sobol index (SI_T), which can offer valuable information. On the one hand, the SI_1 measures the main effects of a parameter on the output variable. It evaluates the contribution of an individual input parameter itself, disregarding interactions with other parameters. The higher the SI_1 value, the greater the impact of this

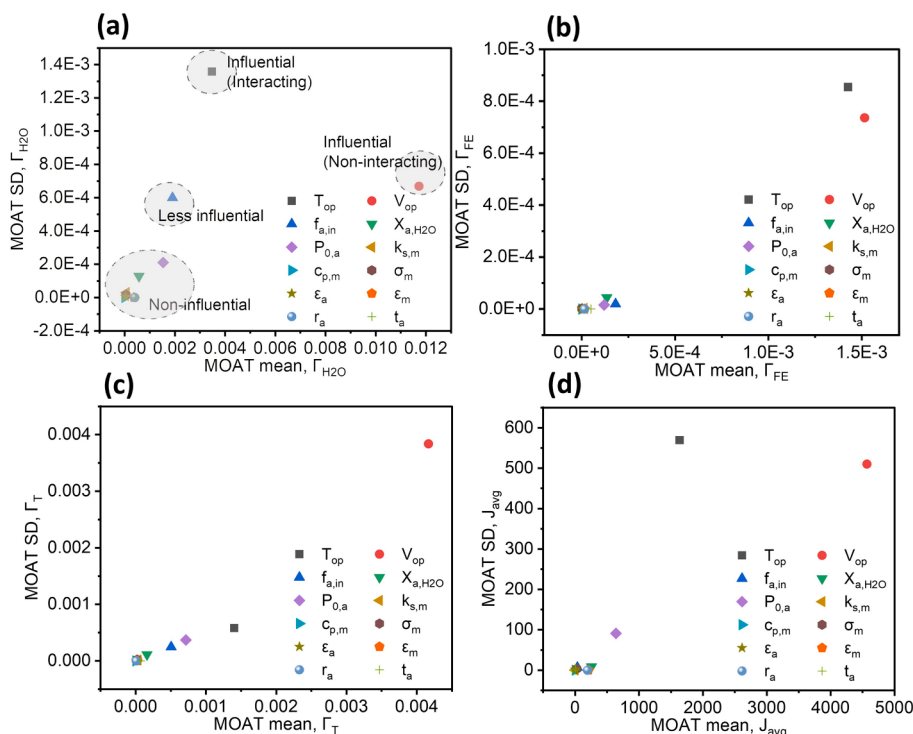


Fig. 3. MOAT mean and standard deviation (SD) of (a) Γ_{H2O} ; (b) Γ_{FE} ; (c) Γ_T ; (d) J_{avg} .

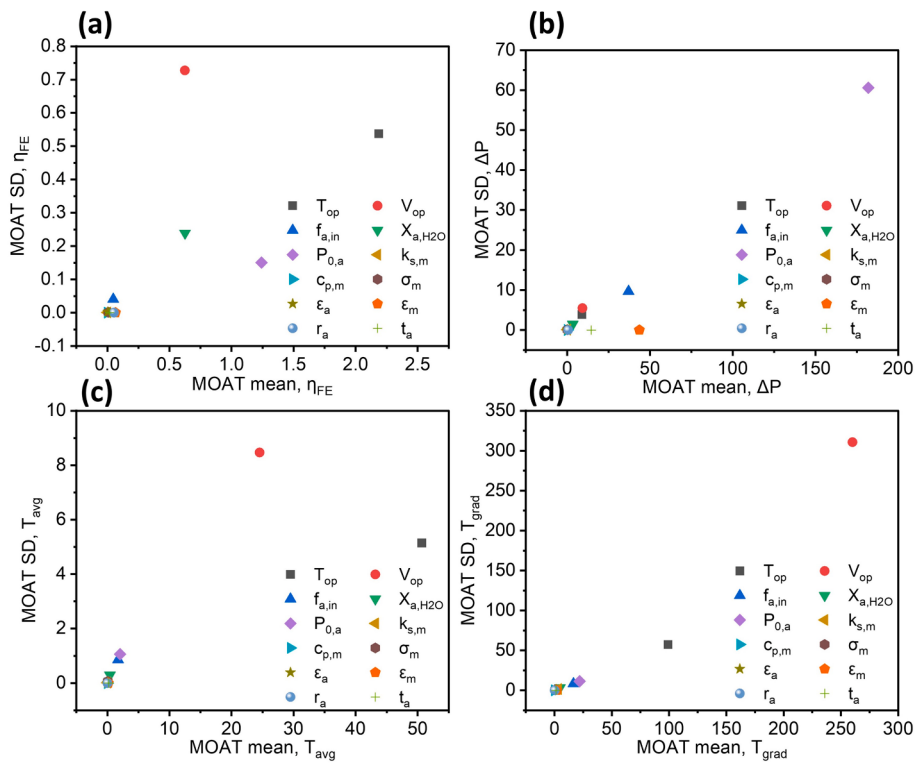


Fig. 4. MOAT mean and standard deviation of (a) η_{FE} ; (b) ΔP ; (c) T_{avg} ; (d) T_{grad} .

Table 6
Screened parameters.

Performance indicators (units)	Influential parameters
J_{avg} ($A\ cm^{-2}$)	V_{op} , T_{op} , $P_{0,a}$
η_{FE} (%)	V_{op} , T_{op} , $X_{a,H2O}$, $P_{0,a}$
T_{avg} ($^{\circ}C$)	V_{op} , T_{op}
T_{grad} ($K\ cm^{-1}$)	V_{op} , T_{op}
ΔP (Pa)	$P_{0,a}$, $f_{a,in}$
Γ_{FE} (1)	V_{op} , T_{op}
Γ_T (1)	V_{op} , T_{op}
Γ_{H2O} (1)	V_{op} , T_{op} , $f_{a,in}$

parameter on the output. This suggests its importance in determining the system's behaviour. On the other hand, the SI_T assesses the overall effects of a parameter, including its main effects as well as interactions with other parameters. Therefore, it provides a comprehensive measure of the parameter's impact on the outputs. Furthermore, the second-order Sobol index (SI_2) can be utilized to measure the interaction effects between two input parameters on the outputs. A higher SI_2 value indicates a stronger interaction between the two parameters.

Fig. 5(a) reveals that the operating voltage and the inlet temperature are the primary factors that notably influence the applied current density. This observation aligns with expectations and suggests that careful control of these parameters is crucial for achieving desired current density levels. Surprisingly, the analysis also indicates that the operating pressure has a greater influence on the PCEC compared to the inlet steam fraction at the anode. This finding highlights the importance of maintaining well-controlled operating pressures, especially when pure steam is used as the feed for the PCEC system. When determining the optimal operating pressure, considerations would be given to the kinetic energy loss from the pump. This perspective ensures a comprehensive evaluation of the PCEC system, considering factors beyond solely maximizing current density. Fig. 6(a) reveals significant interaction effects between voltage and both the inlet temperature and operating pressure. Fig. 5(b) demonstrates that the SI_{T_s} of different factors are greater than the SI_{I_s} ,

indicating the presence of strong interaction effects among variables on the η_{FE} of the PCEC stack (Fig. 6(b)). This finding suggests that the η_{FE} of the PCEC stack can be influenced by a combination of multiple operating factors, rather than being solely dependent on a single factor. This also indicates that compared to the current density, η_{FE} is a more complex performance metric, highlighting the intricate nature of PCEC system. Various operating factors can have a significant impact on the η_{FE} , emphasizing the need to consider multiple factors simultaneously when optimizing and controlling the PCEC stack. Furthermore, in practical applications where the thermal-neutral voltage (TNV) is applied to the PCEC and inlet temperature is kept constant, Fig. 5(b) indicates that controlling the inlet flow rate is the most effective means of enhancing the η_{FE} of PCEC. This finding suggests that, under these specific operating conditions, manipulating the flow rate has the greatest effect on improving η_{FE} [61]. Furthermore, Fig. 5(c)–(e) and Fig. 6(c)–(e) demonstrates that the remaining three performance metrics are solely dependent on specific operating parameters, with negligible interactions observed between different operating parameters. As mentioned earlier, when the operating voltage and inlet temperature are fixed at the TNV in a PCEC system, the operating pressure emerges as the most influential factor for these performance metrics.

In summary, the sensitivity analysis yields three main findings: Firstly, the faradaic efficiency exhibits greater complexity compared to other performance metrics in the PCEC system. It is influenced not only by individual operating parameters but also by their interactions. Secondly, while the inlet temperature and operating voltage hold significant influence over the PCEC stack, practical operations with fixed values for these parameters highlight the increasing importance of controlling and optimizing the operating pressure and inlet flow rate. Lastly, when determining the optimal operating pressure and inlet flow rate, careful consideration should be given to the perspective of the PCEC system, considering their impacts on the energy efficiency of whole system. These findings emphasize the need for a comprehensive understanding of the PCEC system's behaviour and the thoughtful selection of operating parameters to enhance overall performance.

Fig. 7 depicts the Pearson correlation coefficient relating different

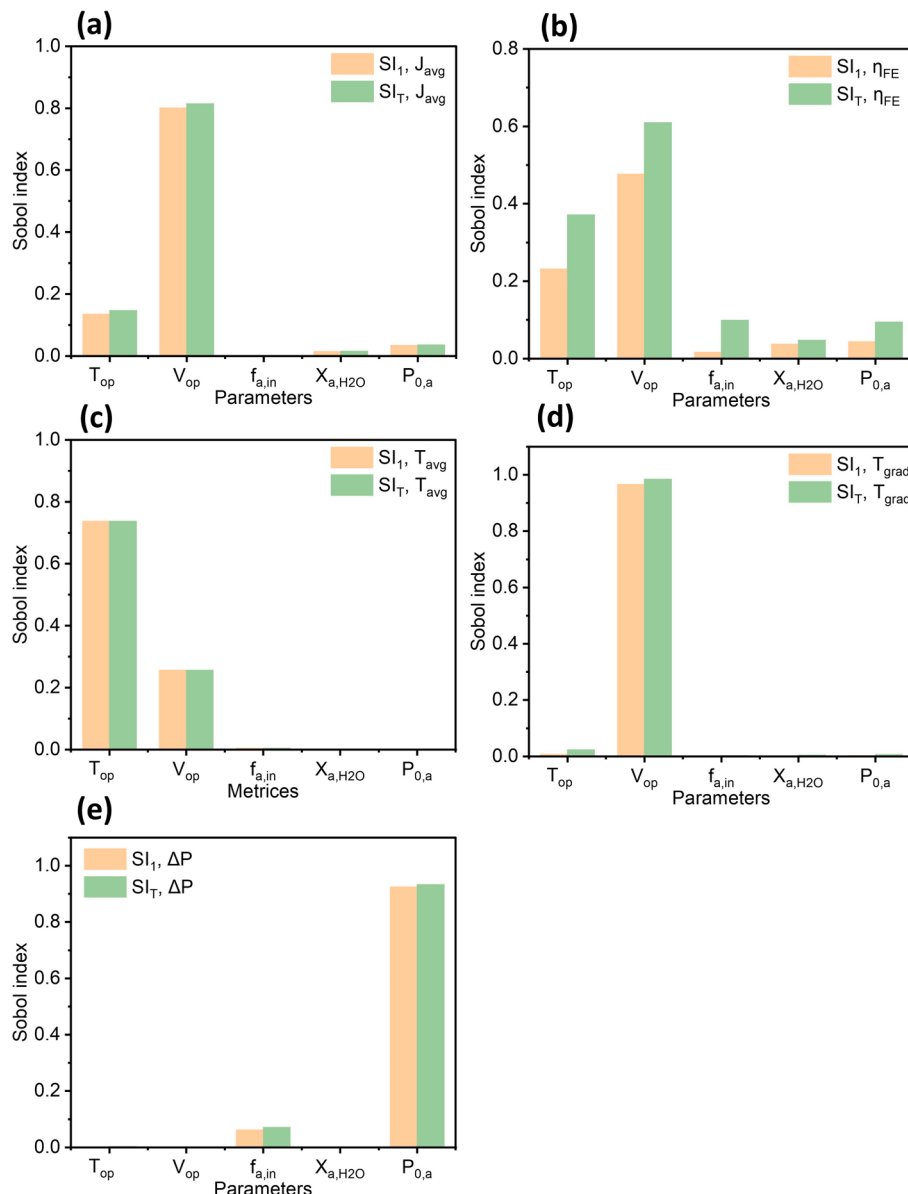


Fig. 5. First-order Sobol index (SI_1) and total Sobol index (SI_T) of (a) J_{avg} ; (b) η_{FE} ; (c) T_{avg} ; (d) T_{grad} ; (e) ΔP .

operational inputs to performance metrics. The operational voltage exhibits the most robust positive correlation with J_{avg} , T_{avg} , and T_{grad} , aligning with the insights from the Sobol indices. Essentially, as the operational voltage rises, so do J_{avg} , T_{avg} , and T_{grad} . Conversely, the most pronounced negative correlation exists between the operational voltage and faradaic efficiency. Consequently, faradaic efficiency diminishes as the operational voltage increases. Furthermore, increasing steam fraction notably boosts the faradaic efficiency. Hence, conducting a Pearson correlation coefficient analysis proves valuable in unravelling the connections between inputs and outputs.

3.3. Performance distribution

The uncertainties in the different input parameters presented in Table 4 can propagate to the outputs. Fig. 8 demonstrates the influence of input uncertainties on each performance indicator, providing a comprehensive overview of the impact on PCECs. In Fig. 8, the y-axis indicates the probability associated with specific values of the performance indicator. A higher value of the density estimate on the y-axis indicates a greater probability of occurrence for that value of

performance indicator. In addition, Table 7 collects the mean and standard deviation of outputs. Compared to other performance metrics, pressure drop, and average temperature demonstrate much higher standard deviations. This indicates that the values for pressure drop and average temperature differ more from the average, implying greater uncertainties. The faradaic efficiency and current density display a more stable distribution in response to changes in the different inputs. This indicates that the values of current density and faradaic efficiency are less affected by changes in the input parameters and exhibit a more consistent behaviour.

In previous studies, the temperature gradient has been identified as a critical parameter. Maintaining a temperature gradient below a certain threshold is essential for ensuring cell performance. Typically, 10 K cm^{-1} is considered as a commonly used guideline in these studies [40,62]. Adhering to this threshold helps to avoid excessive temperature variations within the cell, which can lead to detrimental effects such as cell degradation or even failure. According to this safe threshold for the temperature gradient, the calculated probability of the temperature gradient exceeding this threshold is determined to be 11.39 %.

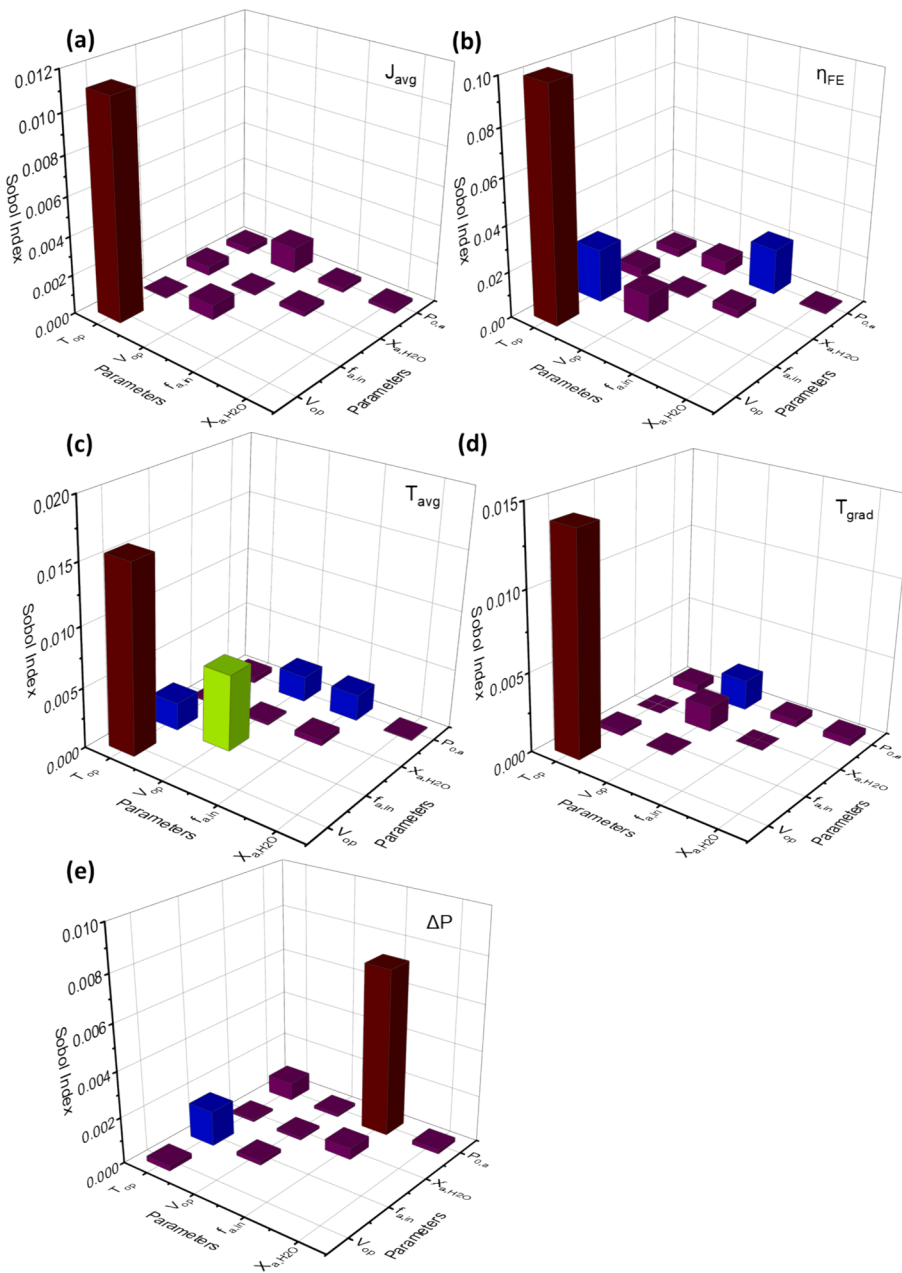


Fig. 6. Second-order Sobol index (SI₂) of (a) J_{avg} ; (b) η_{FE} ; (c) T_{avg} ; (d) T_{grad} ; (e) ΔP .

4. Conclusions

This work aims to attain a deep understanding of the impacts of different input parameters on a metal foam based PCEC stack. A set of 12 operating, structural, microstructural, and material input parameters are selected. Additionally, a set of 8 output parameters are chosen as outputs. In addition, a 3D numerical model is developed for training a DNN-boosted surrogate model.

In the Morris screening step, the five operating parameters (operating temperature/anode pressure/voltage and anode inlet steam fraction/flow rate) are identified as influential parameters based on the results of MOAT mean and standard deviation. Furthermore, three distribution uniformity indices are found to be insensitive to variations in the input parameters. As a result, these indices are not taken into consideration in the subsequent studies. The effects of various operating conditions on the different performance metrics are quantified via the sensitivity analysis. Apart from the pressure drop, the operating

temperature, operating voltage, and their interaction are identified as having significant impacts on the other four performance metrics. Therefore, the results from the sensitivity analysis are important for researchers to optimize the operation strategy to improve the PCEC's performance. Furthermore, the distributions of various performance indicators to the uncertainties in the inputs are provided. Given a threshold of 10 K cm^{-1} , it is determined that there is an 88.61 % probability of metal foam based PCEC stack operating below this threshold.

Overall, this work provides a thoroughly comprehension of a metal foam based PCEC stack operation. The insights gained from the results provide valuable knowledge for comprehending the behaviour of the PCEC stack and devising operating strategies to optimize its performance. Moreover, the workflow and presented surrogate model are promising to be applied to other problems in PCEC, further advancing its development.

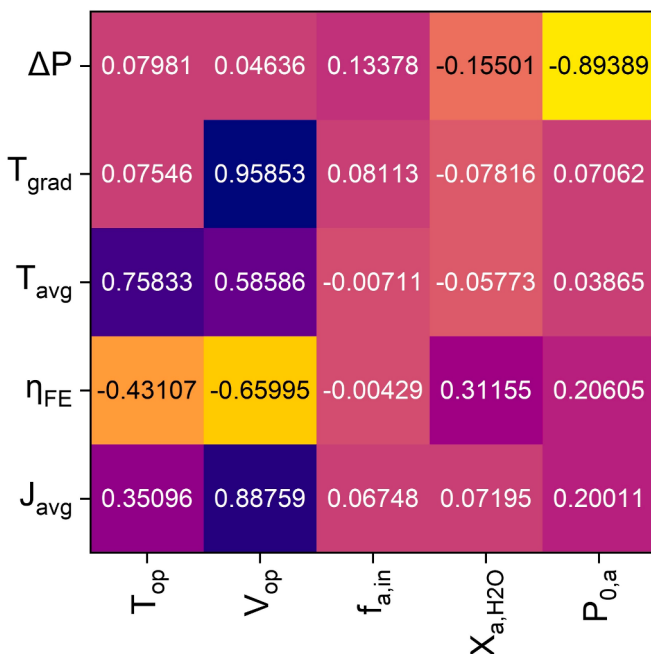


Fig. 7. Pearson correlation coefficient between different parameters and the performance metrics.

CRediT authorship contribution statement

Zheng Li: Writing – original draft, Visualization, Validation, Software, Methodology, Investigation, Formal analysis, Data curation, Conceptualization. **Chen Wang:** Writing – review & editing, Methodology, Investigation, Formal analysis. **Xi Chen:** Writing – review & editing, Validation, Formal analysis. **Na Yu:** Writing – review & editing, Visualization, Validation. **Lei Xing:** Writing – review & editing, Supervision. **Jin Xuan:** Writing – review & editing, Supervision. **Minfang Han:** Writing – review & editing, Supervision, Project administration, Funding acquisition, Formal analysis. **Meng Ni:** Writing – review & editing, Validation, Supervision, Resources, Project administration, Funding acquisition, Formal analysis, Conceptualization.

Declaration of competing interest

The authors declare that they have no known competing financial interests or personal relationships that could have appeared to influence

Table 7
Mean, standard deviation of outputs.

Performance indicators (units)	Mean	Standard deviation
J_{avg} (A cm^{-2})	0.68	0.15
η_{FE} (%)	96.90	0.81
T_{avg} ($^{\circ}\text{C}$)	589.45	19.12
T_{grad} (K cm^{-1})	5.43	3.49
ΔP (Pa)	150.83	24.48

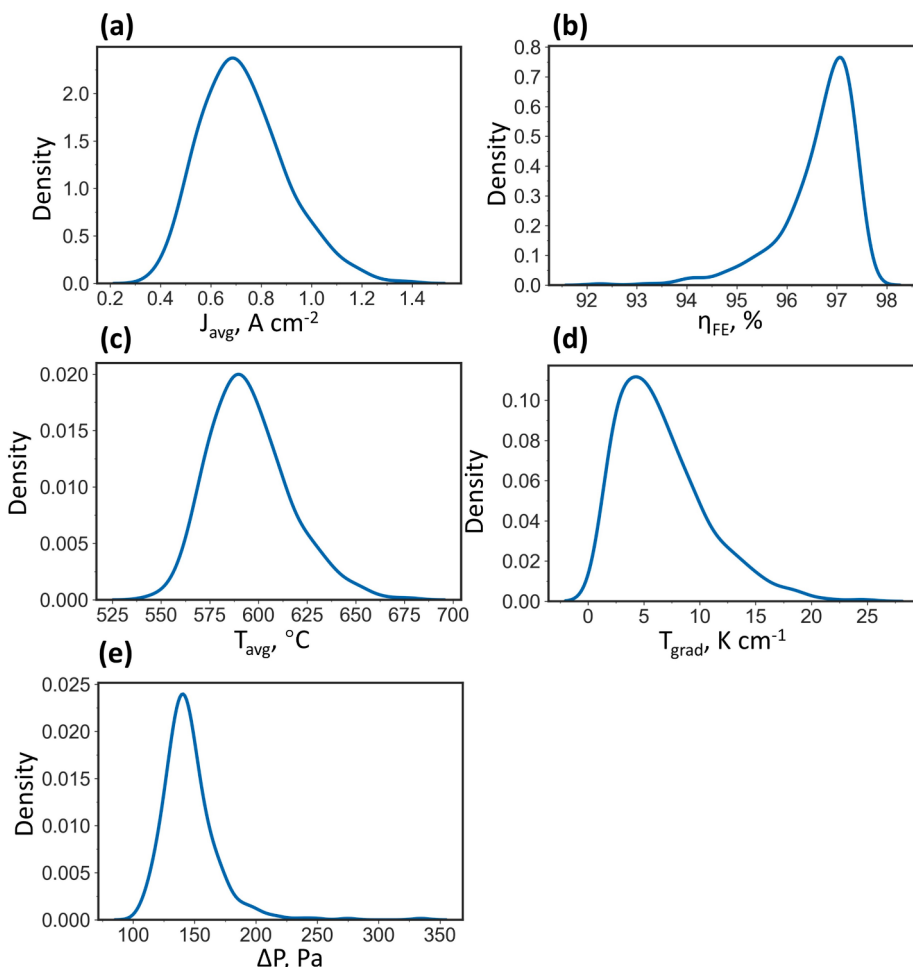


Fig. 8. Density estimates of (a) J_{avg} ; (b) η_{FE} ; (c) T_{avg} ; (d) T_{grad} ; (e) ΔP .

the work reported in this paper.

Data availability

Data will be made available on request.

Acknowledgments

M. NI thanks the grant (Project Number: 15306723 and SRFS2324-5S02) from Research Grants Council, University Grants Committee, Hong Kong SAR.

References

- [1] Patyk A, Bachmann TM, Brisse A. Life cycle assessment of H₂ generation with high temperature electrolysis. *Int J Hydrogen Energy* 2013;38:3865–80. <https://doi.org/10.1016/j.ijhydene.2013.01.063>.
- [2] Yu J, Li Z, Wang C, Xu X, Liu T, Chen D, et al. Engineering advanced noble-metal-free electrocatalysts for energy-saving hydrogen production from alkaline water via urea electrolysis. *J Colloid Interface Sci* 2024;661:629–61. <https://doi.org/10.1016/j.jcis.2024.01.183>.
- [3] Yu J, Li Z, Liu T, Zhao S, Guan D, Chen D, et al. Morphology control and electronic tailoring of CoxAy (A = P, S, Se) electrocatalysts for water splitting. *Chem Eng J* 2023;460:141674. <https://doi.org/10.1016/j.cej.2023.141674>.
- [4] Li Z, Zhang H, Xu H, Xuan J. Advancing the multiscale understanding on solid oxide electrolysis cells via modelling approaches: A review. *Renew Sustain Energy Rev* 2021;141:110863. <https://doi.org/10.1016/j.rser.2021.110863>.
- [5] Vidas L, Castro R. Recent developments on hydrogen production technologies: state-of-the-art review with a focus on green-electrolysis. *Appl Sci* 2021;11:11363. <https://doi.org/10.3390/app112311363>.
- [6] Bhandari R, Trudewind CA, Zapp P. Life cycle assessment of hydrogen production via electrolysis – a review. *J Clean Prod* 2014;85:151–63. <https://doi.org/10.1016/j.jclepro.2013.07.048>.
- [7] Li Z, He Q, Wang C, Yu N, Bello IT, Guo M, et al. Protonic ceramic fuel cells for power-ethylene cogeneration: A modelling study on structural parameters. *Energy* 2023;264:126193. <https://doi.org/10.1016/j.energy.2022.126193>.
- [8] Duan C, Huang J, Sullivan N, O'Hayre R. Proton-conducting oxides for energy conversion and storage. *Appl Phys Rev* 2020;7:011314. <https://doi.org/10.1063/1.5135319>.
- [9] Kim J, Sengodan S, Kim S, Kwon O, Bu Y, Kim G. Proton conducting oxides: A review of materials and applications for renewable energy conversion and storage. *Renew Sustain Energy Rev* 2019;109:606–18. <https://doi.org/10.1016/j.rser.2019.04.042>.
- [10] Bello IT, Guan D, Yu N, Li Z, Song Y, Chen X, et al. Revolutionizing material design for protonic ceramic fuel cells: Bridging the limitations of conventional experimental screening and machine learning methods. *Chem Eng J* 2023;477:147098. <https://doi.org/10.1016/j.cej.2023.147098>.
- [11] Chen X, Yu N, Bello IT, Guan D, Li Z, Liu T, et al. Facile anion engineering: A pathway to realizing enhanced triple conductivity in oxygen electrodes for reversible protonic ceramic electrochemical cells. *Energy Storage Mater* 2023;63:103056. <https://doi.org/10.1016/j.ensm.2023.103056>.
- [12] Bello IT, Song Y, Yu N, Li Z, Zhao S, Maradesa A, et al. Evaluation of the electrocatalytic performance of a novel nanocomposite cathode material for ceramic fuel cells. *J Power Sources* 2023;560:232722. <https://doi.org/10.1016/j.jpowsour.2023.232722>.
- [13] Li W, Shi Y, Luo Y, Cai N. Theoretical modeling of air electrode operating in SOFC mode and SOEC mode: The effects of microstructure and thickness. *Int J Hydrogen Energy* 2014;39:13738–50. <https://doi.org/10.1016/j.ijhydene.2014.03.014>.
- [14] Bessler WG, Gewies S, Willich C, Schiller G, Friedrich KA. Spatial distribution of electrochemical performance in a segmented SOFC: A combined modeling and experimental study. *Fuel Cells* 2010;10:411–8. <https://doi.org/10.1002/fuce.200900083>.
- [15] Xia L, Ni M, He Q, Xu Q, Cheng C. Optimization of gas diffusion layer in high temperature PEMFC with the focuses on thickness and porosity. *Appl Energy* 2021;300:117357. <https://doi.org/10.1016/j.apenergy.2021.117357>.
- [16] Ahmed DH, Sung HJ, Bae J. Effect of GDL permeability on water and thermal management in PEMFCs—I. Isotropic and anisotropic permeability. *Int J Hydrogen Energy* 2008;33:3767–85. <https://doi.org/10.1016/j.ijhydene.2008.04.024>.
- [17] Al-Baghdadi MARS, Al-Janabi HAKS. Modeling optimizes PEM fuel cell performance using three-dimensional multi-phase computational fluid dynamics model. *Energ Conver Manage* 2007;48:3102–19. <https://doi.org/10.1016/j.enconman.2007.05.007>.
- [18] Toghiani S, Afshari E, Baniasadi E. Metal foams as flow distributors in comparison with serpentine and parallel flow fields in proton exchange membrane electrolyzer cells. *Electrochim Acta* 2018;290:506–19. <https://doi.org/10.1016/j.electacta.2018.09.106>.
- [19] Wei Q, Fan L, Tu Z. Hydrogen production in a proton exchange membrane electrolysis cell (PEMFC) with titanium meshes as flow distributors. *Int J Hydrogen Energy* 2023;48:36271–85. <https://doi.org/10.1016/j.ijhydene.2023.06.052>.
- [20] Wan Z, Sun Y, Yang C, Kong X, Yan H, Chen X, et al. Experimental performance investigation on the arrangement of metal foam as flow distributors in proton exchange membrane fuel cell. *Energ Conver Manage* 2021;231:113846. <https://doi.org/10.1016/j.enconman.2021.113846>.
- [21] Zhao J, Lin Z, Zhou M. Three-dimensional modeling and performance study of high temperature solid oxide electrolysis cell with metal foam. *Sustainability* 2022;14:7064. <https://doi.org/10.3390/su14127064>.
- [22] Wang Y, Du Y, Ni M, Zhan R, Du Q, Jiao K. Three-dimensional modeling of flow field optimization for co-electrolysis solid oxide electrolysis cell. *Appl Therm Eng* 2020;172:114959. <https://doi.org/10.1016/j.aplthermaleng.2020.114959>.
- [23] Zielke P, Wulff AC, Sun X, Jensen SH, Kiebach R, Frandsen HL, et al. Investigation of a spinel-forming Cu-Mn foam as an oxygen electrode contact material in a solid oxide cell single repeating unit. *Fuel Cells* 2017;17:730–4. <https://doi.org/10.1002/fuce.201700005>.
- [24] Han Y, Guo M, Sun A, Liu H, Xiao G, Sun Y, et al. Towards feasible temperature management and thermo-mechanical stability of carbon-assisted solid oxide electrolysis cell. *Energ Conver Manage* 2023;276:116483. <https://doi.org/10.1016/j.enconman.2022.116483>.
- [25] Matsuo H, Murakami T, Otomo J. Experimental analyses for electronic structure of barium zirconate-strontium zirconate proton-conducting solid solution. *J Am Ceram Soc* 2021;104:5740–9. <https://doi.org/10.1111/jace.17935>.
- [26] Son MJ, Kim MW, Virkar AV, Lim H-T. Locally developed electronic conduction in a yttria stabilized zirconia (YSZ) electrolyte for durable solid oxide fuel cells. *Electrochim Acta* 2020;353:136450. <https://doi.org/10.1016/j.electacta.2020.136450>.
- [27] Karyofylli V, Danner Y, Ashoke Raman K, Kungl H, Karl A, Jodat E, et al. Sensitivity analysis and uncertainty quantification in predictive modeling of proton-exchange membrane electrolytic cells. *J Power Sources* 2024;600:234209. <https://doi.org/10.1016/j.jpowsour.2024.234209>.
- [28] Kannan V, Xue H, Raman KA, Chen J, Fisher A, Birgersson E. Quantifying operating uncertainties of a PEMFC – Monte Carlo-machine learning based approach. *Renew Energy* 2020;158:343–59. <https://doi.org/10.1016/j.renene.2020.05.097>.
- [29] Shao Q, Gao E, Mara T, Hu H, Liu T, Makradi A. Global sensitivity analysis of solid oxide fuel cells with Bayesian sparse polynomial chaos expansions. *Appl Energy* 2020;260:114318. <https://doi.org/10.1016/j.apenergy.2019.114318>.
- [30] Radaideh MI, Radaideh MI. Efficient analysis of parametric sensitivity and uncertainty of fuel cell models with application to SOFC. *Int J Energy Res* 2020;44:2517–34. <https://doi.org/10.1002/er.4837>.
- [31] Gholaminezhad I, Jafarpur K, Paydar MH, Karimi G. Multi-scale multi-objective optimization and uncertainty analysis of methane-fed solid oxide fuel cells using Monte Carlo simulations. *Energ Conver Manage* 2017;153:175–87. <https://doi.org/10.1016/j.enconman.2017.10.011>.
- [32] Salehi Z, Gholaminezhad I. Multi-objective modeling, uncertainty analysis, and optimization of reversible solid oxide cells. *Int J Energy Environ Eng* 2018;9:295–304. <https://doi.org/10.1007/s40095-018-0269-5>.
- [33] Blatman G, Sudret B. An adaptive algorithm to build up sparse polynomial chaos expansions for stochastic finite element analysis. *Probab Eng Mech* 2010;25:183–97. <https://doi.org/10.1016/j.probengmech.2009.10.003>.
- [34] Samel W, Montavon G, Lapuschkin S, Anders CJ, Muller K-R. Explaining deep neural networks and beyond: a review of methods and applications. *Proc IEEE* 2021;109:247–78. <https://doi.org/10.1109/JPROC.2021.3060483>.
- [35] Yao W, Zheng X, Zhang J, Wang N, Tang G. Deep adaptive arbitrary polynomial chaos expansion: A mini-data-driven semi-supervised method for uncertainty quantification. *Reliab Eng Syst Saf* 2023;229:108813. <https://doi.org/10.1016/j.ress.2022.108813>.
- [36] Zhang F, O'Donnell LJ. Chapter 7 - Support vector regression. In: Mechelli A, Vieira S, editors. *Machine Learning*. Academic Press; 2020. p. 123–40. <https://doi.org/10.1016/B978-0-12-815739-8.00007-9>.
- [37] Erfani SM, Rajasegarar S, Karunasekera S, Leckie C. High-dimensional and large-scale anomaly detection using a linear one-class SVM with deep learning. *Pattern Recogn* 2016;58:121–34. <https://doi.org/10.1016/j.patcog.2016.03.028>.
- [38] Qu Z, Aravind PV, Boksteen SZ, Dekker NJJ, Janssen AHH, Woudstra N, et al. Three-dimensional computational fluid dynamic modeling of anode-supported planar SOFC. *Int J Hydrogen Energy* 2011;36:10209–20. <https://doi.org/10.1016/j.ijhydene.2010.11.018>.
- [39] Pasaoogullari U, Wang C-Y. Computational fluid dynamics modeling of solid oxide fuel cells. *ECS Proc* 2003;2003-07:1403. https://doi.org/10.1149/200307_1403PV.
- [40] Li Z, He Q, Xia L, Xu Q, Cheng C, Wang J, et al. Effects of cathode thickness and microstructural properties on the performance of protonic ceramic fuel cell (PCFC): A 3D modelling study. *Int J Hydrogen Energy* 2022;47:4047–61. <https://doi.org/10.1016/j.ijhydene.2021.11.022>.
- [41] Li Z, Wang C, Bello IT, Guo M, Yu N, Zhu M, et al. Direct ammonia protonic ceramic fuel cell: A modelling study based on elementary reaction kinetics. *J Power Sources* 2023;556:232505. <https://doi.org/10.1016/j.jpowsour.2022.232505>.
- [42] Li K, Araki T, Kawamura T, Ota A, Okuyama Y. Numerical analysis of current efficiency distributions in a protonic ceramic fuel cell using Nernst-Planck-Poisson model. *Int J Hydrogen Energy* 2020;45:34139–49. <https://doi.org/10.1016/j.ijhydene.2020.09.143>.
- [43] Peters C. *Grain-size Effects in Nanoscaled Electrolyte and Cathode Thin Films for Solid Oxide Fuel Cells (SOFC)*. KIT Scientific Publishing; 2009.
- [44] Li Z, Bello IT, Wang C, Yu N, Chen X, Zheng K, et al. Revealing interactions between the operating parameters of protonic ceramic electrolysis cell: A modelling study. *Appl Energy* 2023;351:121886. <https://doi.org/10.1016/j.apenergy.2023.121886>.
- [45] Duan C, Kee R, Zhu H, Sullivan N, Zhu L, Bian L, et al. Highly efficient reversible protonic ceramic electrochemical cells for power generation and fuel production. *Nat Energy* 2019;4:230–40. <https://doi.org/10.1038/s41560-019-0333-2>.

- [46] Ni M, Leung MKH, Leung DYC. Parametric study of solid oxide steam electrolyzer for hydrogen production. *Int J Hydrogen Energy* 2007;32:2305–13. <https://doi.org/10.1016/j.ijhydene.2007.03.001>.
- [47] Beale SB, Andersson M, Boigues-Muñoz C, Frandsen HL, Lin Z, McPhail SJ, et al. Continuum scale modelling and complementary experimentation of solid oxide cells. *Prog Energy Combust Sci* 2021;85:100902. <https://doi.org/10.1016/j.pecs.2020.100902>.
- [48] Xu Q, Xia L, He Q, Guo Z, Ni M. Thermo-electrochemical modelling of high temperature methanol-fuelled solid oxide fuel cells. *Appl Energy* 2021;291:116832. <https://doi.org/10.1016/j.apenergy.2021.116832>.
- [49] Li Z, He Q, Wang C, Xu Q, Guo M, Bello IT, et al. Ethylene and power cogeneration from proton ceramic fuel cells (PCFC): A thermo-electrochemical modelling study. *J Power Sources* 2022;536:231503. <https://doi.org/10.1016/j.jpowsour.2022.231503>.
- [50] Fu Q, Li Z, Liu Z, Wei W. Performance study of solid oxide fuel cell with Ni-foam indirect internal reformer: Intrinsic reforming kinetics and temperature uniformity. *Chem Eng J* 2023;457:141170. <https://doi.org/10.1016/j.cej.2022.141170>.
- [51] Ni M. 2D thermal modeling of a solid oxide electrolyzer cell (SOEC) for syngas production by H₂O/CO₂ co-electrolysis. *Int J Hydrogen Energy* 2012;37:6389–99. <https://doi.org/10.1016/j.ijhydene.2012.01.072>.
- [52] Crestaux T, Le Maître O, Martinez J-M. Polynomial chaos expansion for sensitivity analysis. *Reliab Eng Syst Saf* 2009;94:1161–72. <https://doi.org/10.1016/j.ress.2008.10.008>.
- [53] Oladyshkin S, Nowak W. Data-driven uncertainty quantification using the arbitrary polynomial chaos expansion. *Reliab Eng Syst Saf* 2012;106:179–90. <https://doi.org/10.1016/j.ress.2012.05.002>.
- [54] Chicco D, Warrens MJ, Jurman G. The coefficient of determination R-squared is more informative than SMAPE, MAE, MAPE, MSE and RMSE in regression analysis evaluation. *PeerJ Comput Sci* 2021;7:e623.
- [55] Yang M, Lim MK, Qu Y, Li X, Ni D. Deep neural networks with L1 and L2 regularization for high dimensional corporate credit risk prediction. *Expert Syst Appl* 2023;213:118873. <https://doi.org/10.1016/j.eswa.2022.118873>.
- [56] Wate P, Coors V, Iglesias M, Robinson D. 7 - Uncertainty assessment of building performance simulation: An insight into suitability of methods and their applications. In: Eicker U, editor. *Urban Energy Systems for Low-Carbon Cities*, Academic Press; 2019, p. 257–87. 10.1016/B978-0-12-811553-4.00007-X.
- [57] Wu C, Ni M, Du Q, Jiao K. Global sensitivity analysis of uncertain parameters based on 2D modeling of solid oxide fuel cell. *Int J Energy Res* 2019;43:8697–715. <https://doi.org/10.1002/er.4869>.
- [58] Andersson M, Streb M, Ko JY, Löfqvist Klass V, Klett M, Ekström H, et al. *J Power Sources* 2022;521:230859. <https://doi.org/10.1016/j.jpowsour.2021.230859>.
- [59] Morris MD. Factorial sampling plans for preliminary computational experiments. *Technometrics* 1991;33:161–74. <https://doi.org/10.1080/00401706.1991.10484804>.
- [60] Paleari L, Movedi E, Zoli M, Burato A, Cecconi I, Errahouly J, et al. Sensitivity analysis using Morris: Just screening or an effective ranking method? *Ecol Model* 2021;455:109648. <https://doi.org/10.1016/j.ecolmodel.2021.109648>.
- [61] Li Z, Wang C, Bello IT, Yu N, Chen X, Xuan J, et al. A comprehensive 3D modelling exploration of a protonic ceramic electrolysis cell stack with metal foam. *J Power Sources* 2024;606:234581. <https://doi.org/10.1016/j.jpowsour.2024.234581>.
- [62] Wu X, Yang D, Wang J, Li X. Temperature gradient control of a solid oxide fuel cell stack. *J Power Sources* 2019;414:345–53. <https://doi.org/10.1016/j.jpowsour.2018.12.058>.